Conference on Modelling Fluid Flow (CMFF'22)
The 18th International Conference on Fluid Flow Technologies
Budapest, Hungary, August 30-September 2, 2022

Direct Numerical Simulation of Shallow Water Breaking Waves Generated by Wave Plate

Shuo LIU[1], Hui WANG[2], Annie-Claude BAYEUL-LAINE[3] Olivier COUTIER-DELGOSHA[4]

[1] Corresponding Author. Univ. Lille, CNRS, ONERA, Arts et Métiers Institute of Technology, Centrale Lille, UMR 9014 – LMFL – Laboratoire de Mécanique des Fluides de Lille – Kampé de Fériet, F-59000, Lille, France. Tel.: +33 784 539 404, E-mail: shuo.liu@ensam.eu
[2] Univ. Lille, CNRS, ONERA, Arts et Métiers Institute of Technology, Centrale Lille, UMR 9014 – LMFL – Laboratoire de Mécanique des Fluides de Lille – Kampé de Fériet, F-59000, Lille, France. E-mail: hui.wang@ensam.eu
[3] Univ. Lille, CNRS, ONERA, Arts et Métiers Institute of Technology, Centrale Lille, UMR 9014 – LMFL – Laboratoire de Mécanique des Fluides de Lille – Kampé de Fériet, F-59000, Lille, France. E-mail: annie-claude.bayeul-laine@ensam.eu
[4] Virginia Tech, Kevin T. Crofton Dept. of Aerospace & Ocean Engineering, 460 Old turner street, Blacksburg, VA, 24061, USA. E-mail: ocoutier@vt.edu

ABSTRACT

We present direct numerical simulation of breaking waves in shallow water generated by the wave plate. The open-source Basilisk solver is used to solve the incompressible, variable-density, two-phase Navier-Stokes equations with surface tension. The air-water interface is advected using a momentum-conservative Volume-of-Fluid (MC-VOF) scheme. The surface tension is treated with the balanced-force technique. Adaptive mesh refinement (AMR) scheme is employed for computational efficiency, concentrating the computational resource on the significant solution area. By reconstructing the piston-type wave plate numerically, we realize high-fidelity simulation of experimental waves under the wide-ranging motions of the wave plate. The relationship between varying maximum wave plate speed and associated maximum wave height before breaking is investigated, the onset of wave breaking as a function of the ratio of wave height to water depth is determined to distinguish between non-breaking waves, spilling breakers, and plunging breakers. A typical plunging breaking wave with a large ratio of wave height to water depth is initialized to recognize the wave breaking and air entrainment process. We obtain good collapse of the simulated free-surface evolution and velocity fields with respect to the experiment. The shape and size of air entrapped at impact by plunging jet matches closely the experimental observation during wave breaking. The time-evolving energy budget and bubble characteristics under breaking waves are further discussed based on the numerical results.

Keywords: air entrainment, direct numerical simulation, two-phase flow, wave breaking

NOMENCLATURE

E	$[J]$	energy
S	$[m]$	wavemaker stroke length
ϵ	$[J/s]$	viscous dissipation rate
μ	$[Pa \cdot s]$	dynamic viscosity
ρ	$[kg/m^3]$	fluid density
σ	$[N/m]$	surface tension coefficient
A	$[m^2]$	area of ingested bubbles
c	$[-]$	volume fraction
d	$[m]$	still water depth
f	$[m]$	wavemaker frequency
H	$[m]$	maximum wave height before breaking
L	$[m]$	numerical domain size
l	$[-]$	maximum level of refinement
$N(t)$	$[-]$	number of bubbles
t_{im}	$[s]$	the time of jet impact
u	$[m/s]$	fluid velocity
V_{max}	$[m/s]$	maximum wave plate velocity

Subscripts and Superscripts

k, p, m, d	kinetic, potential, mechanical, and dissipative energy
x, z	streamwise, vertical direction
$1, 2$	phase 1, water; phase 2, air

1. INTRODUCTION

Wave breaking has sparked a lot of research interest due to its importance in upper ocean dynamics and air-sea interactions. The experimental investigations of breaking waves by Duncan [1] and Melville [2] initiated the exploration in the physics that governs their instability, breaking onset, and strength. Progress has been made in several areas, including the prediction of their geometry, breaking onset, energy dissipation, and mechanisms of air entrainment in breaking waves. The turbulence directly associated with breaking is dominant in mixing processes beneath the free surface, making it crucial for transfer of heat, mass, and momentum [3]. However splashing, turbulence, and air entrainment make theoretical modeling challenging once a wave breaks. Field measurement using various detection methods have difficulty quantifying wave breaking due to the strongly nonlinear intermittent breaking process and environmental influences [4]. Controlled laboratory experiment and numerical modelling are able to isolate and analyze the impact of wave breaking on a variety of fundamental air-sea interfacial properties, measuring the scaling relationships between the surface wave field and the kinematics and dynamics of breaking [5, 6]. The measurements of breaking waves generated by wave plate provide general entrainment processes visualized by high speed imaging and the temporal evolution of turbulence quantified using particle image velocimetry (PIV), but present many technical challenges in terms of measuring temporo-spatial evolution and resolving both the large and small structures simultaneously during the wave breaking processes. Therefore direct numerical simulation (DNS) becomes a feasible method for solving complex breaking process which spans a wide range of scales, allowing researchers to gain a better understanding of the physical role played by the entrained air bubbles in basic processes such as wave energy dissipation. The numerical methodology followed in this investigation involves the simulation of incompressible flow of two immiscible fluids. The Navier-Stokes equations are solved numerically on sufficiently fine grids to retain the effect of viscosity and surface tension, allowing the physical properties of breaking waves to be accurately captured.

2. NUMERICAL SCHEME AND PROBLEM DESCRIPTION

2.1. Basilisk Solver

We solve the gas-liquid two-phase incompressible Navier-Stokes equations with variable density and surface tension using the Basilisk library. The Basilisk package is an open-source program for the solution of a wide variety of partial differential equation systems on regular adaptive Cartesian meshes. The incompressible, variable density Navier-Stokes equations with surface tension can be written as:

$$\rho(\partial_t \boldsymbol{u} + (\boldsymbol{u} \cdot \nabla)\boldsymbol{u}) = -\nabla p + \nabla \cdot (2\mu \boldsymbol{D}) + \boldsymbol{f}_\sigma \qquad (1)$$

$$\partial_t \rho + \nabla \cdot (\rho \boldsymbol{u}) = 0 \qquad (2)$$

$$\nabla \cdot \boldsymbol{u} = 0 \qquad (3)$$

With $\boldsymbol{u} = (u, v, w)$ the fluid velocity, $\rho \equiv \rho(x, t)$ the fluid density, p the pressure, $\mu \equiv \mu(x, t)$ the dynamic viscosity, D the deformation tensor defined as $D_{ij} \equiv (\partial_i u_j + \partial_j u_i)/2$, and f_σ the surface tension force per unit volume [7].

The liquid-gas interface is tracked by the momentum-conserving volume-of-fluid (MCVOF) advection scheme [8] combined with quad/octree adaptive mesh refinement (AMR) method, while the corresponding volume fraction field is solved by a piecewise-linear geometrical scheme [9] together with a balanced-force continuous-surface-force model for the surface tension. The generic time loop and a CFL-limited timestep are used for the implementation of the numerical scheme. The momentum equation is projected using the Bell-Colella-Glaz advection scheme [10], and the viscous terms are solved implicitly. Gravity is taken into account using the "reduced gravity approach" [11].

2.2. momentum-conserving VOF method

The VOF method was originally developed by Hirt & Nichols (1981) [12] and has been modified by Kothe *etal*. (1991) [13], and further coupled with momentum conservation by Fuster & Popinet (2018) [8], with the advantage of allowing variable spatial resolution and sharp representation along the interface, while limiting the appearance of spurious numerical parasitic currents caused by momentum leakage between the dense and light phases [8, 14]. A function $c(x, t)$, defined as the volume fraction of a particular fluid in each cell of the computational mesh, assuming values of 0 or 1 for each phase, is used to reconstruct the interface of two-phase flow. The density and viscosity can thus be calculated using arithmetic means as follows:

$$\rho(c) = \alpha\rho_1 + (1 - c)\rho_2 \qquad (4)$$

$$\mu(c) = \alpha\mu_1 + (1 - c)\mu_2 \qquad (5)$$

with ρ_1, ρ_2, and μ_1, μ_2 the density and viscosity of the first and second fluids, respectively.

The advection equation for the density can be substituted with an equivalent advection equation for the volume fraction:

$$\partial_t c + \nabla \cdot (c\boldsymbol{u}) = 0 \qquad (6)$$

The piecewise linear interface construction (PLIC) approach is applied. The interface normal is computed by the Mixed-Youngs-Centered (MYC) method [15] and the position of the interface in the cell is determined using the method of Scardovelli & Zaleski (2000)[16].

Momentum conserving scheme in the advective momentum fluxes near the interface has been proved to be essential to reduce numerical momentum transfer through the interface, especially for cases with large density difference of the two phases. Total fluxes on each face are obtained by adding the diffusive flux due to the viscous term, which are computed by semi-implicit Crank-Nicholson scheme [17]. The Bell-Collela-Glaz (BCG) second-order upwind scheme is used for the reconstruction of the liquid and gas momentum per unit volume to be advected in the cell.

2.3. balanced-force surface tension formulation

Surface tension forces can be important for capturing main cavity at impact and wave hydrodynamics during post-breaking process. Surface tension is treated with the method of Brackbill *etal*. (1992)[18] and the balanced-force technique [19] as further developed by Popinet (2009, 2018) [20, 21]. To solve the inconsistency at low interface resolution, a generalized version of the height-function (HF) curvature estimation is used, resulting in accurate and efficient surface-tension-driven flow solutions.

3. PROBLEM DESCRIPTION AND MODEL VALIDATION

3.1. Problem description

A series of breaking wave experiments have been conducted in the Department of Mechanical Engineering of Johns Hopkins University in a $6m$ long, $0.3m$ wide, and $0.6m$ high wave flume with the aim to study the dispersion of oil spills by breaking waves [22, 23]. The breaking waves are initialized by driving a piston-type wavemaker over a uniform water depth d=0.25m. A single wave breaking event was generated by a single push of the wavemaker, and its trajectory $x(t)$ and associated wave plate velocity $v(t)$ are determined by following function:

$$x(t) = \frac{S}{2}(1 - cos(2\pi f t)), 0 \leq t \leq \frac{f}{2} \tag{7}$$

$$v(t) = S\pi f cos(2\pi f t), 0 \leq t \leq \frac{f}{2} \tag{8}$$

where S is the wavemaker stroke length, f is the frequency, and t is the time.

On the basis of the laboratory experiments, we perform 2D simulations of breaking waves using Basilisk solver. A plunging breaking wave with S=0.5334m and f=0.75Hz has been selected for detailed study, resulting in maximum wave plate velocity of $V_{max} = A\pi f = 1.26m/s$. Furthermore, Parameterization was performed to relate the wave characteristics to the initial conditions by varying the stroke S and frequency f. We define that x represent the streamwise direction, and z is the vertical direction, positive upward, and measured from the still water level. (see Figure 1).

A constant depth of water for the interface $\eta(x,z)_{(t=0)} = d$, with d the still water depth, is used as initial condition in a square box of size $L = 6m$. The wave propagates in the x direction. Based on direct numerical simulations of the water-air mixture result-

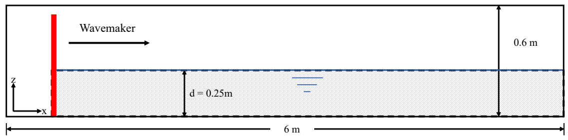

Figure 1. Sketch of laboratory breaking wave experiment and numerical domain.

ing from the entrainment of bubbles due to breaking, we intend to investigate the mechanisms of breaking waves in terms of free-surface profiles, time-evolving energy budget and bubble characteristics.

3.2. parameter space

The density and viscosity ratios of the two phases are those of air and water in the experiments, which are $1.29/1018.3$ and $17.9e-6/1.01e-3$, respectively. The Reynolds number in the breaking waves generated by the wave plate can be defined by $Re = \rho V_{max} S/\mu$, with ρ the density of water, V_{max} the maximum wave plate velocity, and S the stroke length [24]. The surface tension can be expressed by the Weber number $We = \rho u_{max}^2 S/\sigma$, with σ the constant surface tension coefficient between water and air. The numerical resolution is given by $\Delta = L/2^l$, where l is the maximum level of refinement in the AMR scheme. The maximum level of refinement, which depends on the minimum size of particles that needs to be resolved in the breaking waves, is 15 in this study, corresponding to a minimum mesh size of $122\mu m$. The surface tension scheme is time-explicit so the maximum timestep is the oscillation period of the smallest capillary wave. For maximum level of refinement $l = 15$, the corresponding maximum timestep should not be larger than $6.4e-5$. To ensure numerical stability, we require the CFL number to be varied in accordance with the various stages of wave breaking evolution, generally decreasing from 0.5 to 0.3. The refinement criterion is based on wavelet-estimated discretization error in terms of the velocity, vorticity or VOF fields [25]. In this study, the refinement criteria on the VOF tracers and velocity field components are used for adaptive refinement to capture the water-air interface and the immersed boundary of the wave plate. The refinement algorithm is invoked every timestep and refines when the wavelet estimated error exceeds $u_{err} = 1e-3$ for velocity field and $f_{err} = 1e-6$ for volume fraction field. For the plunging breaking wave with $S = 0.5334m$ and $f = 0.75Hz$, due to the limitation of computational resources, combined with the decreasing effects of Reynolds number on the evolution of wave breaking, we choose $Re = 1 \times 10^5$, this value of Reynolds number corresponds to a maximum wave plate velocity of $0.51m/s$ and a water depth of $0.08m$, which are smaller than 5-6 order of magnitude of actual values. We expect that Reynolds-number effects should not fundamentally alter the basic nature of the scaling we have derived [26]. We use the physical value of water

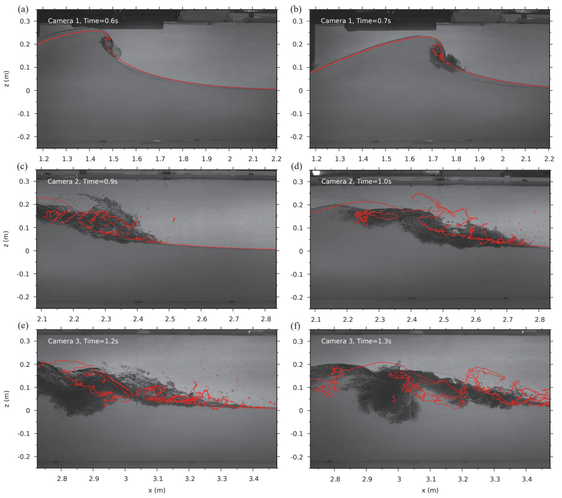

Figure 2. Comparison of free surface profile between laboratory images and numerical results

surface tension coefficient with air, $\sigma = 0.0728 kg/s^2$, to analyze the effect of surface tension on the formation of main cavity, it gives $We = 12000$.

3.3. Breaking waves validation

3.3.1. Breaking waves profiles

Three high-speed cameras with a frame rate of 500 frames per second were used in the experiments to visualize the development of wave breaking and subsequent breakup processes. The fields of view, 103×103, 75×75, and 75×75 cm^2, are centered horizontally at x=1.66, 2.43, and 3.07m for cameras 1, 2, and 3, respectively. The vertical center of all cameras are adjusted to the initial free surface. We compare numerical results of interface evolution over time for a plunging breaker generated by a motion of wave plate with $S = 0.5334m$ and $f = 0.75$ to experimental snapshots from high-speed cameras. Comparisons of free surface profile between simulation results and snapshots taken during the experiments are shown in Figure 2.

Camera 1, located upstream of the wave direction, close to the side of the wave plate, is primarily responsible for recording the development of plunging jet, jet impact and air entrainment, and the generation of the first splash-up. As shown in Fig. 2(a) and Fig. 2(b), comparisons of the free surface evolution at $t = 0.6s$ and $0.7s$ show a great agreement between the current simulation and the experimental results from Camera 1. As the wave slope becomes steeper and wave crest curls over, The plunging jet can be observed at $t = 0.6s$, with the tendency to project downward to the water surface. At $t = 0.7s$ the plunging jet impacts onto the rising wave front, forming the main cavity by entrapping a tube of air. During this process, the evolution of the free surface, including the curvature of the overturning wave crest, the size of the main cavity, and the height and location of the first splash-up, can be accurately predicted by our numerical simulations. The numerical simulation closely predicted the evolution of the free surface, including the height and position of wave crest, curvature of overturning wave crest, and the precise size of main cavity, and the height and position of the first splash-up.

The subsequent development of the initial wave crest and first splash-up were recorded by Camera 2. At $t = 0.9s - 1.0s$, because of the propagation of the perturbations and capillaries at the main free surface prior to the impact of the first splash-up, the free surface beneath the ligaments and droplets of the first splash-up has already been disturbed (c). Following that, the first splash-up dives and connects with the free surface (d). The initial wave crest weakens, the main cavity expands and ruptures, generating a large number of small bubbles, and then floats to the vicinity of the free surface due to buoyancy. During this process, more abundant water droplets and ligaments were observed in the experiment, as indicated by the black region in the experimental snapshots. Our grid scale is fine enough to capture the formation of water droplets, air bubbles, and ligaments, but these phenomena can not be fully acquired using the present 2D numerical simulation.

Some differences are observed in the simulated free surface evolution compared to the snapshots taken by Camera 3. In Comparison to the experimental observations, we find the similar phenomena of the occurrence and rising of second splash-up (e), and the decaying wave crest still looks similar, but the exact development of the second splash-up and rising wave front are not be reproduced by our numerical simulation. It appears to be a phase shift in the distribution of the bubble cloud region (f), but the similar size of the bubble cloud region and penetration depth under the water can be obtained. These discrepancies can be explained by the fact that a slight perturbation at the wave front eventually leads to the development of drastically different breaking processes, this chaotic behavior of breaking waves has been investigated across several runs with the same laboratory setup, demonstrating a non-repeatable breaking process particularly in the post-breaking region[27].

To sum up briefly, A good agreement regarding the wave shape and maximum wave height before breaking is obtained, and the simulated size of main cavity entrapped by the plunging jet is almost the same compared to that of experiment. Some differences can be seen in the location after wave breaking. The generation of water droplets, air bubbles, and ligaments is inaccurate, the profiles wave front and the distribution of the bubble cloud region can not be well reproduced. This can be explained by the lack of bubbles and droplets generation due to the absence of 3D effect, and the chaotic behavior of breaking waves in the post-breaking region.

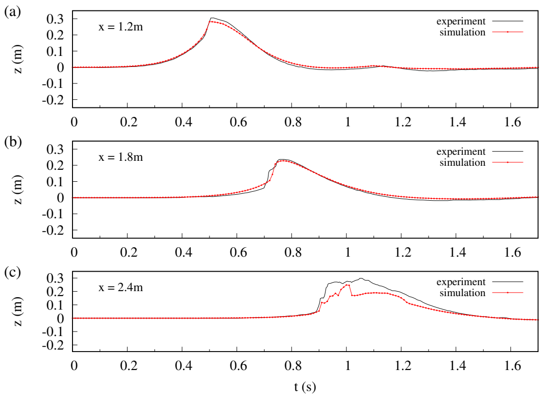

Figure 3. Comparison of surface elevations over time at x = 1.2m (a), 1.8m (b), and 2.4m (c)

3.3.2. The evolution of surface elevation over time

Figure 3. shows the simulated free-surface profiles over time recorded at three designated positions (x = 1.2m, 1.8m, and 2.4m) corresponding to the pre-breaking, breaking, and post-breaking regions, respectively, with a comparison to the experimental high-speed imaging results.

The free-surface profile at the first position (x = 1.2m) remains approximately smoothly curved, which corresponds to the pre-breaking stage where the free-surface is smooth, with no vertical interface formation and the generation of bubbles and droplets (a). The numerical simulation accurately reproduces the evolution of the free surface, including the development of the rise and fall of the wave profile, with only a slight underestimation (0.02m, 6.7% error) at the peak value of the wave profile at t = 0.5s. The possible reason for the discrepancy is the The second position is located at x = 1.8m, within the wave breaking region, near the main cavity entrapped by plunging jet. we notice that in the experiment, the free-surface appears an immediate rising after jet impact at around t = 0.7s, indicating the penetration of the plunging jet into the wave front and the formation of the main cavity. Fig. 3(b) shows that our numerical simulation can closely capture the phenomenon of how wave breaks. The only discrepancy can be caused by the lack of the production of small splash when the plunging jet penetrates into the wave front due to the absence of 3D effect. The wave propagates to the third position and develops into the turbulent flow, forming a large amount of spray and bubbles. There are apparent fluctuation of the free-surface between t = 0.9s and 1.4s, showing the strongly turbulent phenomenon during this region. Fig. 3(c) shows a overall underestimation of the free surface elevations from t = 0.9s to 1.4s by our numerical simulation. This is most likely due to differences in the recording of free surface elevations between the experiment and numerical simulation. The value of free surface elevations in the experiment is the maximum elevation of wave profile, splashing bubbles and droplets, as the free surface elevations are recorded from the black region in the experimental snapshots. However, in the numerical simulation, the free surface elevations are primarily determined by wave profiles rather than splashing droplets scattered above the water surface. In general, the temporal evolution of free-surface profiles can be precisely reproduced by our simulation when compared to laboratory experiments at each location. Despite the limitations of the 2D simulation in producing droplets and ligaments in the spanwise direction, the ability of our model to capture wave hydrodynamics, including accurate reproduction of wave height, wave speed, and wave breaking process, can be demonstrated through the comparisons above.

4. DISCUSSIONS

4.1. Relationship between wave height and maximum wave plate speed

We develop relationships to connect maximum wave height before breaking H with maximum wave plate speed used for generating our waves, which is $V_{max} = A\pi f$ in this study. We restrict consideration to air-water systems close to standard temperature and pressure. The relationship between H and V_{max} has been investigated by conducting various cases with different V_{max}. The influence of Reynolds number on the resulting wave height has also been demonstrated by using distinct values of Re = 10^5 and $Re = 6 \times 10^5$. Figure 4. illustrates the relationship between H and V_{max} normalized by d and the shallow water wave speed, $(gd)^{1/2}$, respectively. As is evident, the data collapses onto a single line. As V_{max} increases, the regular wave becomes to break, and the breaking process changes from spilling to plunging. Our numerical result underestimates the wave height, and the difference between them increases with increasing V_{max}. The assumption that the flow becomes independent of the Reynolds number for sufficiently large values of Re can be validated from here. The transition between regular and breaking waves, the spilling and plunging breaker happens to be around H/d = 0.65 and H/d = 0.80, respectively. It is very close to the measurement done by Li (2017) [22], who showed that the critical value for spilling and plunging wave is H/d = 0.8.

A linear correlation between maximum wave height before breaking H and maximum wave plate speed V_{max} has been revealed, showing that wave height becomes higher as the maximum wave speed increases. The resulting wave heights between two regimes with distinct Re values are quite consistent, but are slightly smaller than the experiment results. It indicates that we can expect that the evolution of wave profiles with time is independent on the Reynolds number.

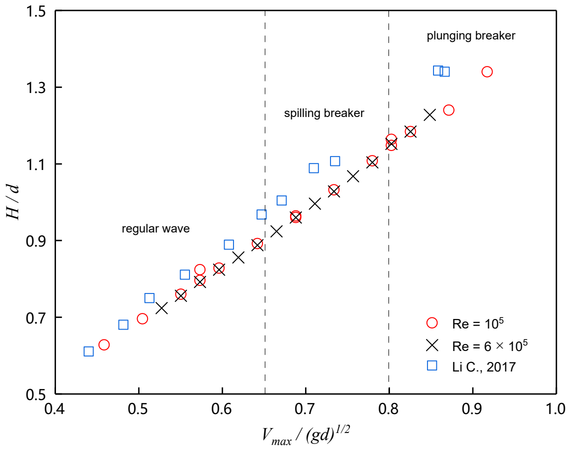

Figure 4. Relationship between maximum wave height before breaking H and maximum wave plate speed V_{max}

4.2. Energy budget

We present an energy budget after jet impact and analyze energy decay and viscous dissipation due to breaking. The time histories of the kinetic E_k, potential E_p and total mechanical energy E_m are shown in Figure 5. The total mechanical energy of the wave is calculated as the sum of the kinetic and potential components $E_m = E_k + E_p$. Data are non-dimensionalized using the associated initial values at the time of jet impact t_{im}.

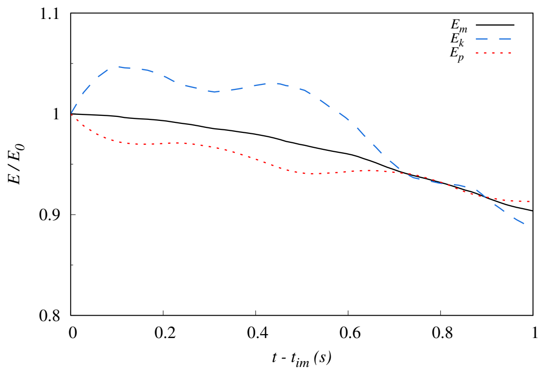

Figure 5. Time histories of the kinetic E_k, potential E_p and total mechanical energy E_m

Starting from the initial impact of plunging jet, there are two visible energy transfers between kinetic and potential energy, leading to two apparent splash-up productions. As the wave breaking progresses, the wave crest diminishes, the plunging jet strikes the free surface and penetrates into the water, E_k rapidly increases and E_p begins to decline until the first and second splash-ups occur at $t - t_{im} = 0.1s$ and $t - t_{im} = 0.45s$, respectively. When splash-up starts rising, E_k, which has achieved its maximum, begins to decline, transferring to potential energy. The total energy decays gradually with a continuously increasing decay rate over this breaking phase. In the later stage of breaking waves, notably after $t - t_{im} = 0.65s$, the wave becomes more turbulent, the total mechanical energy exhibits a greater decay due to substantial air-water mixing and vortical structures.

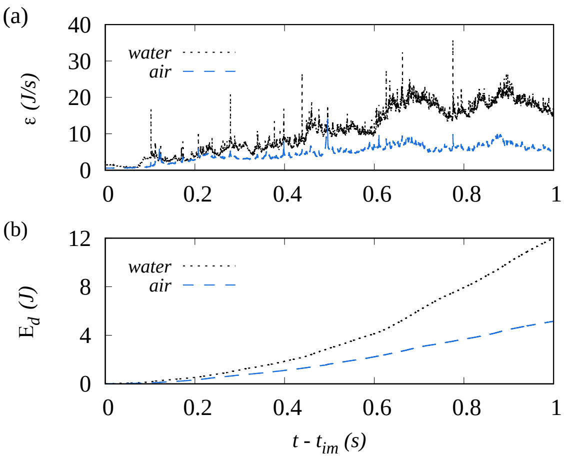

Figure 6. time histories of the viscous dissipation rate ϵ (a) and corresponding dissipation E_d (b)

Figure 6. depicts the time histories of the viscous dissipation rate ϵ and the corresponding dissipation E_d. Since we compute the breaking waves in 2D simulation, we consider the width of spanwise direction as a unit. The dissipation rate in both water and air is markedly intermittent, with strong synchronization of their fluctuations over time. We note that the occurrence of maximum dissipation rate fluctuations is closely related to the exchange time of energy transfer, i.e. the moments when E_k and E_p reach their extreme values. With the development of breaking process, the dissipation rate in water increases greatly, while the dissipation rate in air remains steady (a). The time when the viscous dissipation gradient in water increases significantly coincides roughly to the moment of splash-up productions, and the viscous dissipation in water increases continuously until $t - t_{im} = 1s$ with no evident reduction in dissipation rate observed. The majority of dissipation is caused by air in the early stages after breaking, and subsequently dissipation due to water dominates the energy dissipation as the increasing dissipation rate in water (b).

4.3. bubble entrainment

Wave breaking injects a large amount of air into the water by the entrainment of bubbles, which is distinguished by a wide distribution of bubble sizes. The 2D numerical studies in the breaking wave literature may not able to investigate accurate bubble size distributions, but the evolution of their formation and breakup processes can be generally captured by fine grid scales through DNS, as can be seen in Figure 7., which shows the time histories of the number of bubbles $N(t)$ and total ingested area to water normalized by main cavity size A/A_0.

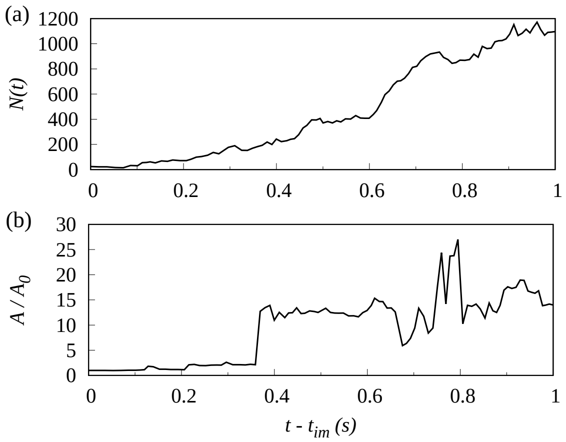

Figure 7. Time histories of the number of bubbles $N(t)$ (a) and the total ingested area of bubbles to water normalized by main cavity size A/A_0 (b)

The first bubble can be identified at the moment when plunging jet impact t_{im}, which is also referred to as the main cavity initially ingested in the breaking process. Subsequently, the first splash-up develops and penetrates into the water, with the main cavity being squeezed and distorted, generating lots of small bubbles. During this period, the total number of bubbles $N(t)$ begins to increase, but the total ingested area of bubbles has no significant increase. Then the total ingested bubbles spikes to a higher size at around $t - t_{im} = 0.37s$, this abrupt increase is associated with the behavior that the first splash-up impacts on and connects to the free surface. A similar phenomenon occurs for the second splash-up around $t - t_{im} = 0.67s$. It shows that the bubble size enclosed by the first and second splash-up is more than ten times that of the main cavity. We also observe the transient collapse in the total ingested area of bubbles caused by the intermittent rupture and reconnecting of the ligaments on the top face of the splash-ups (b). As shown in Fig. 7(a), There is a roughly constant production rate at $0.1s$ that lasts until $0.6s$, and then a rapid increase in the number of bubbles, which correlates with the breakup of the main cavity due to the turbulence around the cavity. It's worth noting that the temporal development of the number of bubbles shows a high similarity to the viscous dissipation rate during the breaking process, implying that there could be a link between the number of bubbles and energy dissipation rate.

5. SUMMARY

We have presented 2D direct numerical simulations of breaking waves in shallow water generated by the wave plate using Basilisk to solve the two-phase Navier-Stokes equations with surface tension. The high-fidelity modeling of experimental waves has been achieved by reconstructing the piston-type wave plate numerically to provide precise information on the hydrodynamics and energetics of the breaker as well as statistics for bubble productions. For the relationship between varying maximum wave plate speed and associated maximum wave height before breaking, we have investigated the onset of wave breaking in terms of the ratio of wave height to water depth, and determined critical values for the transition between non-breaking waves, spilling breakers, and plunging breakers. For a typical plunging breaking wave with a large ratio of wave height to water depth, We obtain good collapse of the free-surface profiles and entrapped air characteristics with respect to the experiment, showing the ability to resolve wave hydrodynamics and breaking process over a large scale separation. We present a time-evolving energy budget to analyze the energy transfer and decay due to breaking, showing an intermittent and growing viscous dissipation rate induced by air-water mixing and vortical structures in the post-breaking stage. The corresponding relationship between bubble statistics and the breaking process has also been investigated, revealing a strong association between the number of bubbles and energy dissipation rate.

ACKNOWLEDGEMENTS

This work has been supported by the scholarship from China Scholarship Council (CSC) under the Grant CSC No. 201906090270. Computations were performed using computational resources on Advanced Research Computing (ARC) at Virginia Tech.

REFERENCES

[1] Duncan, J., 1981, "An experimental investigation of breaking waves produced by a towed hydrofoil", *Proceedings of the Royal Society of London A Mathematical and Physical Sciences*, Vol. 377 (1770), pp. 331–348.

[2] Melville, W., 1982, "The instability and breaking of deep-water waves", *Journal of Fluid Mechanics*, Vol. 115, pp. 165–185.

[3] Banner, M., and Peregrine, D., 1993, "Wave breaking in deep water", *Annual Review of Fluid Mechanics*, Vol. 25 (1), pp. 373–397.

[4] Melville, W. K., 1996, "The role of surface-wave breaking in air-sea interaction", *Annual review of fluid mechanics*, Vol. 28 (1), pp. 279–321.

[5] Perlin, M., Choi, W., and Tian, Z., 2013, "Breaking waves in deep and intermediate waters", *Annual review of fluid mechanics*, Vol. 45, pp. 115–145.

[6] Derakhti, M., Kirby, J. T., Banner, M. L., Grilli, S. T., and Thomson, J., 2020, "A unified breaking onset criterion for surface gravity water waves in arbitrary depth", *Journal of Geophysical Research: Oceans*, Vol. 125 (7), p. e2019JC015886.

[7] Deike, L., Melville, W. K., and Popinet, S., 2016, "Air entrainment and bubble statistics in breaking waves", *Journal of Fluid Mechanics*, Vol. 801, pp. 91–129.

[8] Fuster, D., and Popinet, S., 2018, "An all-Mach method for the simulation of bubble dynamics problems in the presence of surface tension", *Journal of Computational Physics*, Vol. 374, pp. 752–768.

[9] Scardovelli, R., and Zaleski, S., 1999, "Direct numerical simulation of free-surface and interfacial flow", *Annual review of fluid mechanics*, Vol. 31 (1), pp. 567–603.

[10] Bell, J. B., Colella, P., and Glaz, H. M., 1989, "A second-order projection method for the incompressible Navier-Stokes equations", *Journal of computational physics*, Vol. 85 (2), pp. 257–283.

[11] Wroniszewski, P. A., Verschaeve, J. C., and Pedersen, G. K., 2014, "Benchmarking of Navier–Stokes codes for free surface simulations by means of a solitary wave", *Coastal Engineering*, Vol. 91, pp. 1–17.

[12] Hirt, C. W., and Nichols, B. D., 1981, "Volume of fluid (VOF) method for the dynamics of free boundaries", *Journal of computational physics*, Vol. 39 (1), pp. 201–225.

[13] Kothe, D. B., Mjolsness, R. C., and Torrey, M. D., 1991, *RIPPLE: A computer program for incompressible flows with free surfaces*, Available to DOE and DOE contractors from OSTI.

[14] Zhang, B., Popinet, S., and Ling, Y., 2020, "Modeling and detailed numerical simulation of the primary breakup of a gasoline surrogate jet under non-evaporative operating conditions", *International Journal of Multiphase Flow*, Vol. 130, p. 103362.

[15] Aulisa, E., Manservisi, S., Scardovelli, R., and Zaleski, S., 2007, "Interface reconstruction with least-squares fit and split advection in three-dimensional Cartesian geometry", *Journal of Computational Physics*, Vol. 225 (2), pp. 2301–2319.

[16] Scardovelli, R., and Zaleski, S., 2000, "Analytical relations connecting linear interfaces and volume fractions in rectangular grids", *Journal of Computational Physics*, Vol. 164 (1), pp. 228–237.

[17] Pairetti, C., Popinet, S., Damián, S., Nigro, N., and Zaleski, S., 2018, "Bag mode breakup simulations of a single liquid droplet", *6th European Conference on Computational Mechanics*.

[18] Brackbill, J. U., Kothe, D. B., and Zemach, C., 1992, "A continuum method for modeling surface tension", *Journal of computational physics*, Vol. 100 (2), pp. 335–354.

[19] Francois, M. M., Cummins, S. J., Dendy, E. D., Kothe, D. B., Sicilian, J. M., and Williams, M. W., 2006, "A balanced-force algorithm for continuous and sharp interfacial surface tension models within a volume tracking framework", *Journal of Computational Physics*, Vol. 213 (1), pp. 141–173.

[20] Popinet, S., 2009, "An accurate adaptive solver for surface-tension-driven interfacial flows", *Journal of Computational Physics*, Vol. 228 (16), pp. 5838–5866.

[21] Popinet, S., 2018, "Numerical models of surface tension", *Annual Review of Fluid Mechanics*, Vol. 50, pp. 49–75.

[22] Li, C., 2017, "Dispersion of Oil Spills by Breaking Waves", Ph.D. thesis, Johns Hopkins University.

[23] Afshar-Mohajer, N., Li, C., Rule, A. M., Katz, J., and Koehler, K., 2018, "A laboratory study of particulate and gaseous emissions from crude oil and crude oil-dispersant contaminated seawater due to breaking waves", *Atmospheric Environment*, Vol. 179, pp. 177–186.

[24] Sumer, B. M., Jensen, P. M., Sørensen, L. B., Fredsøe, J., Liu, P. L.-F., and Carstensen, S., 2010, "Coherent structures in wave boundary layers. Part 2. Solitary motion", *Journal of fluid mechanics*, Vol. 646, pp. 207–231.

[25] Van Hooft, J. A., Popinet, S., Van Heerwaarden, C. C., Van der Linden, S. J., de Roode, S. R., and Van de Wiel, B. J., 2018, "Towards adaptive grids for atmospheric boundary-layer simulations", *Boundary-layer meteorology*, Vol. 167 (3), pp. 421–443.

[26] Mostert, W., and Deike, L., 2020, "Inertial energy dissipation in shallow-water breaking waves", *Journal of Fluid Mechanics*, Vol. 890.

[27] Wei, Z., Li, C., Dalrymple, R. A., Derakhti, M., and Katz, J., 2018, "Chaos in breaking waves", *Coastal Engineering*, Vol. 140, pp. 272–291.